

Polyline Based Generative Navigable Space Segmentation for Autonomous Visual Navigation

Zheng Chen, Zhengming Ding, David Crandall, Lantao Liu

Abstract—Detecting navigable space is a fundamental capability for mobile robots navigating in unknown or unmapped environments. In this work, we treat the visual navigable space segmentation as a scene decomposition problem and propose Polyline Segmentation Variational AutoEncoder Networks (PSV-Nets), a representation learning based framework to enable robots to learn the navigable space segmentation in an unsupervised manner. Current segmentation techniques heavily rely on supervised learning strategies which demand a large amount of pixel-level annotated images. In contrast, the proposed framework leverages a generative model — Variational AutoEncoder (VAE) and an AutoEncoder (AE) to learn a polyline representation that compactly outlines the desired navigable space boundary in an unsupervised way. We also propose a visual receding horizon planning method that uses the learned navigable space and a Scaled Euclidean Distance Field (SEDF) to achieve autonomous navigation without an explicit map. Through extensive experiments, we have validated that the proposed PSV-Nets can learn the visual navigable space with high accuracy, even without any single label. We also show that the prediction of the PSV-Nets can be further improved with a small number of labels (if available) and can significantly outperform the state-of-the-art fully supervised learning based segmentation methods.

I. INTRODUCTION

For mobile robots to navigate in unknown space, it is crucial to understand the traversability of complex environments that consist of cluttered objects. The goal is to construct collision-free traversable space, which we term as *navigable space*. If cameras are used to perceive the environment, a typical way to identify navigable space is through image segmentation by leveraging deep neural networks (DNNs) to perform multi-class [1]–[4] or binary-class [5]–[10] segmentation of images. The present work belongs to the binary-class segmentation case where the robot needs to identify navigable space from streaming images while classifying all other parts, which are usually complex and unstructured, as non-navigable space.

However, most existing DNN-based methods are developed on top of a supervised learning paradigm and rely on annotated datasets such as KITTI [11] or CityScape [12]. These datasets usually contain an immense number of pixel-level annotated segmented images. Collecting and annotating such data for robotic applications in other environments is prohibitively costly and time-consuming, especially for outdoor environments.

To overcome the limitation of fully-supervised learning and pave a path for mobile robot navigation, we propose to develop a self-supervised learning method by treating the binary navigable space segmentation as a scene decomposition problem. It has been demonstrated in [13]–[16] that the scene decomposition can be solved in an unsupervised fashion with Variational AutoEncoders (VAEs). In contrast to semantic segmentation by supervised learning where the model is trained to learn human-annotated pixel-wise labels, scene decomposition attempts to learn the compositional nature from the visual information alone without supervision.

Most, if not all, existing VAE-based scene decomposition and representation learning methods use pixel-wise learning where the value of every pixel is predicted. However, pixel-wise approaches usually ignore dependencies between pixels, which can cause spurious holes, small scattered islands, and irregular shapes [17]. A more compact way to segment/decompose the scene is to use polylines/splines (represented by vertices or control points) to outline individual components [17], [18]. There are several benefits of using vertices-based representations. First, the number of points parameterizing the polylines is significantly less than the number of pixels in an image. Second, as shown in [19]–[21], a vertices-based representation provides an efficient and user-friendly way for possible human-machine interaction. Third, the predicted polyline is an abstract (or intermediate) representation of the environmental structure and it is shown in [22] that predictions on the intermediate representations (e.g., edges) may provide excellent clues for predicting more details, which in our case may lead to an efficient way to predict map structures.

The proposed PSV-Nets (Polyline Segmentation VAE Networks) consist of two networks, Net-I (a VAE) and Net-II (an AE). The goal of Net-I is to learn a pseudo label from surface normals by using categorical distributions as the latent representation. Using supervision signals from Net-I, Net-II learns a set of vertices which describe the location of the navigable space boundary. We then develop a navigation planning method to guide the robot to move without collision.

II. RELATED WORK

Traditional unsupervised image segmentation methods focus on crafting features and energy functions to define desired objectives. One representative framework is the active contour based models [24] which optimize over a polygon (represented by vertices) by means of energy minimization based on both the image features and some shape priors, e.g., boundary continuity and smoothness. However, active

Z. Chen, D. Crandall, L. Liu are with the Luddy School of Informatics, Computing, and Engineering at Indiana University, Bloomington, IN 47408, USA. E-mail: {zcl1, djcran, lantao}@iu.edu.
Z. Ding is with the Department of Computer Science at Tulane University. Email: zding1@tulane.edu
This research is supported by the ARL grant W911NF-20-2-0099

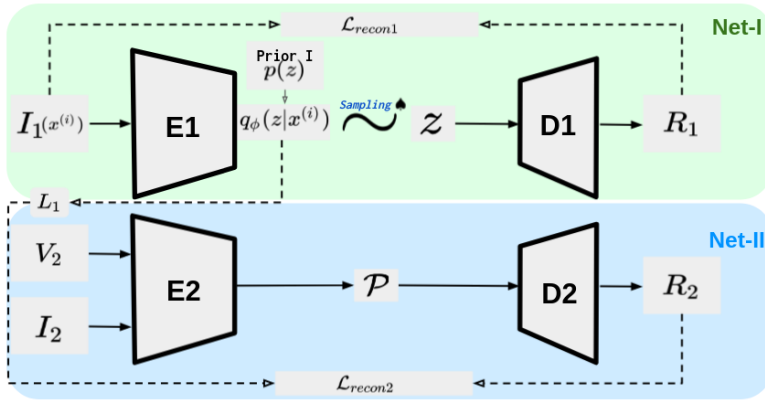


Fig. 1. Framework overview. **Net-I:** I_1 is the input surface normal image. $q_\phi(z|x^{(i)})$ represents the latent categorical distribution from which a segmentation sample z is sampled using \spadesuit – the Gumbel-Softmax sampler for discrete distributions proposed in [23]. Prior I is to regularize the “shape” of the predicted latent distribution. R_1 is the reconstructed input and \mathcal{L}_{recon1} is the mean squared error between I_1 and R_1 . **Net-II:** I_2 is the same as I_1 . V_2 is the initial vertices for polyline representation. $\{P\}$ is a set of predicted vertices from $E2$. R_2 is the reconstructed image and \mathcal{L}_{recon2} is the mean squared error between I_2 and the latent image L_1 , converted from the latent distribution q_ϕ .

contours lack flexibility and heavily rely on low-level image features and global parameterization of priors [25]. Recently, deep active contour based models have been proposed [25]–[28], but these methods require ground-truth contour vertices and thus belong to the supervised learning paradigm. Another line of research uses adversarial approaches for unsupervised segmentation, e.g., work in [29] explores the idea to change the textures or colors of objects without changing the overall distribution of the dataset and proposes an adversarial architecture to segment a foreground object per image. Although the adversarial methods show impressive results, they suffer from instabilities of training. This proposed research is close in spirit to some work in scene decomposition [13]–[15], where the goal is to decompose scenes into objects in an unsupervised fashion with a generative model. However, in contrast to those pixel-wise learning based approaches, our framework adopts a more compact and efficient representation – splines – to outline the boundary of the navigable and non-navigable space.

Our proposed framework is built upon VAEs. The core of VAEs is said in [30] to be well aligned with representation learning [31], which is to learn useful representations of data with little or no supervision. The trained generative model (decoder) can generate new images by taking any random samples from the learned latent distribution. Many variants of VAEs have been proposed following [32], including Conditional-VAE [33], WAE [34], Beta-VAE [35], IWAE [36], Categorical-VAE [23], joint-VAE [37], and VQ-VAE [38], where the latent representation could be described as either a continuous distribution, a discrete distribution, or a combination. In this paper, to learn the navigable space boundary we use two distributions for two AutoEncoders.

In addition, the value of boundaries in image segmentation has been shown in a large amount of previous literature. A polygon/spline representation is used in [18]–[21], [39] to achieve a fast and potentially interactive instance segmentation. Acuna *et al* propose a new approach to learn sharper and more accurate semantic boundaries [40]. By treating boundary detection as the dual task of semantic segmentation, a new loss function with a boundary consistency constraint to improve the boundary pixel accuracy for semantic segmentation is designed [41]. The work in [42] proposes a content-adaptive downsampling technique that

learns to favor sampling locations near semantic boundaries of target classes. By doing so, the segmentation accuracy and computational efficiency can be well balanced. Although the above mentioned methods make use of boundaries to improve the performance, they all require ground-truth labels for training, which is an important limitation that we aim to overcome in this work.

To achieve visual navigation autonomously, learning-based methods have been widely studied recently [43], [44]. For example, imitation learning based approaches have been largely explored to train a navigation policy that enables a robot to mimic human behaviors or navigate close to certain waypoints without a prior map [45], [46]. To fully utilize the known dynamics model of the robot, semi-learning-based scheme is also proposed [44] to combine optimal control and deep neural network to navigate through unknown environments. A large amount of work on visual navigation can also be found in the computer vision community, such as [43], [47]–[50], all of which use full-learning-based methods to train navigation policies, which work remarkably well when training data is sufficient, but can catastrophically fail if no or very limited data is available.

III. METHODOLOGY

A. Navigable Space Segmentation

The proposed PSV-Nets consist of two networks, as shown in Fig. 1. Net-I aims to learn a pixel-wise categorical distribution that describes the spatial layout of navigable space, whereas Net-II is designed to outline the shape of the pixel-wise prediction in Net-I using a set of vertices.

1) *Net-I:* The goal of Net-I is to learn a pseudo label from the input surface normal image. A standard VAE aims to learn a generative model which can generate new data from a random sample in a specified latent space. We want to obtain the parameters of the generative model by maximizing the data marginal likelihood: $\log p_\theta(\mathbf{x}^{(i)})$, where $\mathbf{x}^{(i)}$ is one of data points in our training dataset $\{\mathbf{x}^{(i)}\}_{i=1}^N$. Using Bayes’ rule, the likelihood could be written as:

$$\log p_\theta(\mathbf{x}^{(i)}) = \log \sum_{\mathbf{z}} p_\theta(\mathbf{x}^{(i)}|\mathbf{z})p_\theta(\mathbf{z}), \quad (1)$$

where $p_\theta(\mathbf{z})$ is the prior distribution of the latent representation \mathbf{z} and $p_\theta(\mathbf{x}^{(i)}|\mathbf{z})$ is the generative probability distribution of the reconstructed input given the latent representation. We

can use a neural network (NN) to approximate $p_\theta(\mathbf{x}^{(i)}|\mathbf{z})$ where θ can be thought as parameters of the NN, but we cannot perform the sum operation over \mathbf{z} , hence Eq. (1) is computationally intractable.

An alternative way is to find the lower bound of Eq. (1). To derive a lower bound of Eq. (1), we can use an encoder to approximate the true posterior of latent variable $p_\theta(\mathbf{z}|\mathbf{x}^{(i)})$. We denote the encoder (another NN) as $q_\phi(\mathbf{z}|\mathbf{x}^{(i)})$, where ϕ is a set of parameters of the encoder NN. Then we could derive the lower bound of Eq. (1) as:

$$\log p_\theta(\mathbf{x}^{(i)}) = \mathbb{E}_{\mathbf{z}} \log p_\theta(\mathbf{x}^{(i)}|\mathbf{z}) - \mathbb{KL}(q_\phi(\mathbf{z}|\mathbf{x}^{(i)})||p_\theta(\mathbf{z})) + \mathbb{KL}(q_\phi(\mathbf{z}|\mathbf{x}^{(i)})||p_\theta(\mathbf{z}|\mathbf{x}^{(i)})). \quad (2)$$

In Net-I, to perform the segmentation task, we assume $p_\theta(\mathbf{x}^{(i)}|\mathbf{z}) = \prod_{j=1}^J \mathcal{N}(\mathbf{x}^{(i)}; \hat{\mathbf{x}}_j(\mathbf{z}; \theta), \sigma^2)$, $q_\phi(\mathbf{z}|\mathbf{x}^{(i)}) = \prod_{j=1}^J \text{Cat}(z_j|\mathbf{x}^{(i)}, \phi)$, and the prior $p_\theta(\mathbf{z}) = \prod_{j=1}^J \text{Cat}(z_j)$, where J is the number of pixels in the input image (same meaning in the following sections). Then only the last term $\mathbb{KL}(q_\phi(\mathbf{z}|\mathbf{x}^{(i)})||p_\theta(\mathbf{z}|\mathbf{x}^{(i)}))$ of Eq. (2) is unknown. Fortunately, we know that $\mathbb{KL}(p||q) \geq 0$ is always true for any two distributions p and q . Therefore, we have:

$$\log p_\theta(\mathbf{x}^{(i)}) \geq \mathbb{E}_{\mathbf{z}} \log p_\theta(\mathbf{x}^{(i)}|\mathbf{z}) - \mathbb{KL}(q_\phi(\mathbf{z}|\mathbf{x}^{(i)})||p_\theta(\mathbf{z})), \quad (3)$$

where the term on the right-hand side of \geq is called the *Evidence Lower Bound* (ELBO) of the data marginal likelihood. Maximizing the ELBO is equivalent to maximizing the data marginal likelihood. By utilizing Monte Carlo sampling, the total loss function over the whole training dataset is:

$$\mathcal{L}_1 = \sum_{i=1}^N \mathbb{KL}(q_\phi(\mathbf{z}|\mathbf{x}^{(i)})||p_\theta(\mathbf{z})) + \frac{1}{2K\sigma^2} \sum_{k=1}^K \left\| \mathbf{x}^{(i)} - \hat{\mathbf{x}}(\mathbf{z}_{ik}; \theta) \right\|_2^2 + \frac{J}{2} \log \sigma^2, \quad (4)$$

where N is the number of images in our training dataset and K is the number of samples in Monte Carlo sampling.

2) *Net-II*: With the supervision signals from Net-I, Net-II can learn a set of vertices which describe the location of the navigable space boundary. We use a hybrid net consisting of a convolutional neural network and a graph convolutional network as the encoder (see the *left block*, E2 in Fig. 2). The overall objective of Net-II consists of a reconstruction loss and an appearance matching loss [51]. Specifically, the loss of Net-II, \mathcal{L}_2 , is estimated using the Structural Similarity Index Measure (SSIM) combined with a Mean Squared Error (MSE) between L_1 and R_2 ,

$$\mathcal{L}_2 = \lambda_1 \frac{1 - \text{SSIM}(L_1, R_2)}{2} + \lambda_2 \frac{1}{J} \|L_1 - R_2\|_2^2, \quad (5)$$

where J is the total number of pixels, λ_1 and λ_2 are weights and $\lambda_1 + \lambda_2 = 1$.

Specific Net-II components are described as follows.

Image Feature Extraction (IFE): In Net-II, the IFE module is used to extract deep features of different layers from the input image for each vertex. The coordinates of the vertices are used to pool the features at converted positions by bilinear interpolation since the sizes of different feature images are different from the original one.

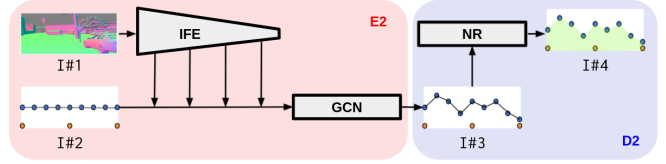


Fig. 2. Structure of Net-II. I#1: Surface normal image; I#2: Initial vertices; I#3: Newly predicted vertices; and I#4: Newly reconstructed image. *Left block*: encoder of Net-II. IFE: Image Feature Extraction net. GCN: Graph Convolutional Network. *Right block*: decoder of Net-II. NR: Neural Rendering module. In both blocks, blue points are vertices of polyline while the orange points are auxiliary points on image bottom boundary for the convenience of neural rendering.

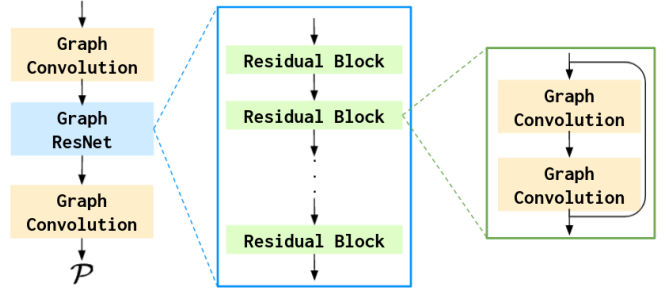


Fig. 3. GCN module in the *left block* of Fig. 2.

Graph Convolution Network (GCN): We construct a graph using the vertices and use the concatenation of the extracted image features and their coordinates as the feature of each node in the graph. Our GCN structure (see Fig. 3) is inspired by the network structure proposed in recent work [21], [52]. The differences are: (a) we do not use graph unpooling layers and (b) we only use 6 graph residual convolution layers in GraphResNet. The fundamental layer of the proposed GCN module is the graph convolution layer. We denote a Graph as $\mathcal{G} = \{\mathcal{V}, \mathcal{E}, \mathcal{F}\}$, where $\mathcal{V} = \{v_i\}_{i=1}^N$ denotes the nodes set, $\mathcal{E} = \{e_j\}_{j=1}^M$ represents the edges set, and $\mathcal{F} = \{f_i\}_{i=1}^N$ is the feature vectors set for nodes in the graph. Then a graph convolution layer is defined as:

$$f_i^{l+1} = \Gamma(w_0^l f_i^l + \sum_{j \in \mathcal{N}(i)} w_j^l f_j^l), \quad (6)$$

where f_i^{l+1} and f_i^l are the feature vectors on vertex i before and after the convolution, $\mathcal{N}(i)$ are the neighboring nodes of node i , and $\Gamma(\cdot)$ is the activation function.

Triangles Selection for Neural Rendering: To convert the vertices predicted from the encoder E2 to a reconstructed image, we triangularize those vertices and select proper triangles for neural rendering. We firstly select three auxiliary vertices on the bottom boundary of image (see orange points of the *left block* of Fig. 2) and form a set of vertices \mathcal{P} . We use Delaunay triangulation to construct triangles on \mathcal{P} . Then we use neural rendering [53] to render \mathcal{P} into a mask while keeping the whole pipeline differentiable. However, a discrepancy exists: Delaunay triangulation always returns a series of triangles forming a convex hull but the shape of real navigable space is not necessarily always convex, so it is

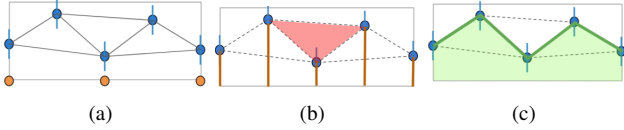


Fig. 4. Triangles selection for neural rendering. (a) Auxiliary points (orange); example predicted vertices (blue); and constructed triangles (black lines, only those formed by boundary points are considered in this step). (b) Orange lines connect predicted vertices with corresponding projected vertices on the image bottom border. Only those triangles who do not intersect with any of orange lines are abandoned (e.g., the red one). (c) Desired navigable space from neural rendering is marked as green region.

possible to render more triangles than needed. We propose to use a simple triangle selection method (see Fig. 4) to filter out those unnecessary triangles. In this process, we assume all the triangles are either above or under the desired navigable space boundary and no triangle crosses the boundary.

B. Visual Navigation

We achieve feasible visual navigation by combining the learned image segmentation with a receding horizon planning mechanism. Specifically, first we compute a library of motion primitives [54], [55] $\mathcal{M} = \{\mathbf{p}_1, \mathbf{p}_2, \dots, \mathbf{p}_n\}$ where each $\mathbf{p}_* = \{\mathbf{x}_1, \mathbf{x}_2, \dots, \mathbf{x}_m\}$ is a single primitive. We use $\mathbf{x}_* = [x \ y \ \psi]^T$ to denote a robot pose. Then we compute the navigation cost function for each primitive based on the evaluation on collision risk and target progress. Finally we select the primitive with minimal cost to execute. The trajectory selection problem can be defined as:

$$\mathbf{p}_{optimal} = \underset{\mathbf{p}}{\operatorname{argmin}} w_1 \cdot C_c(\mathbf{p}) + w_2 \cdot C_t(\mathbf{p}), \quad (7)$$

where $C_c(\mathbf{p}) = \sum_j^m c_c^j$ and $C_t(\mathbf{p}) = \sum_j^m c_t^j$ are the collision cost and target cost of one primitive \mathbf{p} , and w_1, w_2 are corresponding weights, respectively.

1) *Collision Avoidance*: In this work, we propose a Scaled Euclidean Distance Field (SEDF) for obstacle avoidance. Conventional collision avoidance is usually conducted in the map space [56], [57], where an occupancy map and the corresponding Euclidean Signed Distance Field (ESDF) have to be provided in advance or constructed incrementally in real time. In this work instead we eliminate this expensive map construction process and evaluate the collision risk directly in the image space. Specifically, we first compute a SEDF image $E'(S)$ based on an edge map $Edge(S)$ detected in the learned binary segmentation $S(I)$, where I is the input image to our PSV-Nets. We then project the motion primitives from the map space to the image space and evaluate all primitives' projections in $E'(S)$.

To perform obstacle avoidance in image space, we have to detect the obstacle boundary in $Edge(S)$. To achieve this, we propose to categorize the edges in $Edge(S)$ into two classes, *Strong Obstacle Boundaries (SOBs)* and *Weak Obstacle Boundaries (WOBs)*. We treat the boundary from the binary segmentation as a function of a single variable in image space, and we use the twin notions of convexity and concavity of functions to define the SOBs and WOBS, respectively. SOBs mean obstacles are near to the robot (e.g.,

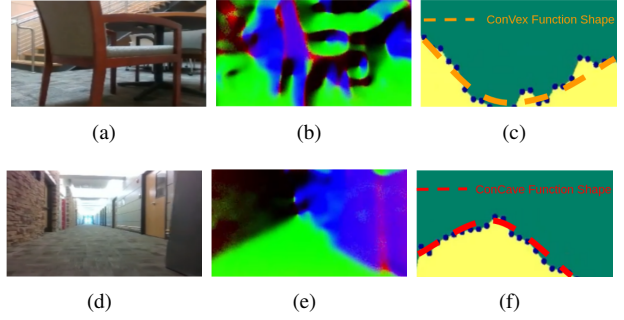


Fig. 5. Images from the camera on a ground robot in a real indoor environment. *Left column*: RGB images; *Middle column*: Surface normal images; *Right column*: Predicted segmentation images (yellow: navigable; green: non-navigable) from our proposed PSV-Nets. Blue dots are sampled points from the predicted boundary. The orange dash line represents an approximated convex function shape while the red dash line is an approximated concave function shape.

the random furniture closely surrounding the robot) and they cause the boundaries to exhibit an approximated *Convex Function Shape (CVFS)* (see Fig. 5(c)). WOBS indicate obstacles are far (compared with SOBs) from the robot (e.g., the wall boundaries that the robot makes large clearance from) and they typically make the boundaries reveal an approximated *Concave Function Shape (CCFS)* (see Fig. 5(f)). In this work, we only consider the obstacles with SOBs and adopt a straightforward way (as in Eq. (8)) to detect boundary segments in $Edge(S)$ with CVFS. We use a points set Ω to represent the boundary segments:

$$\Omega = \{(u, v), (u, v) \in Edge(S) \text{ and } v > v_{thres}\}, \quad (8)$$

where (u, v) are the coordinates in the image frame, as shown in Fig. 6(a), and v_{thres} is a pre-defined value for evaluating the boundary convexity. If we use $\partial\Omega$ to denote the boundary of a set, then in our case we have $\partial\Omega = \Omega$. Then the definition of an EDF is:

$$E[u, v] = d((u, v), \partial\Omega) \quad (9)$$

$$d(x, \partial\Omega) := \inf_{y \in \partial\Omega} d(x, y),$$

where $d(x, y) = \|x - y\|$ is the Euclidean distance between vectors x and y .

However, directly computing an EDF using Eq. (9) in the image space will propagate the obstacles' gradients to the whole image space, which might cause the planning evaluation space to be too limited. To address this, we introduce a scale factor α to compute a corrected version of EDF:

$$E'[u, v] = \begin{cases} E[u, v], & \text{if } E[u, v] \leq \alpha \cdot d_{max} \\ \alpha \cdot d_{max}, & \text{otherwise} \end{cases} \quad (10)$$

where $\alpha \in [0, 1]$, and $d_{max} = \max_{u \in \mathcal{U}, v \in \mathcal{V}} E[u, v]$, where \mathcal{U} and \mathcal{V} are the rows and columns index sets, respectively. Some examples of E' with different α values can be seen in Fig. 6.

Assume \mathbf{x}^j is the j^{th} pose in one primitive and its image coordinates are (u^j, v^j) , then the collision risk for \mathbf{x}^j is

$$c_c^j = E'[u^j, v^j]. \quad (11)$$

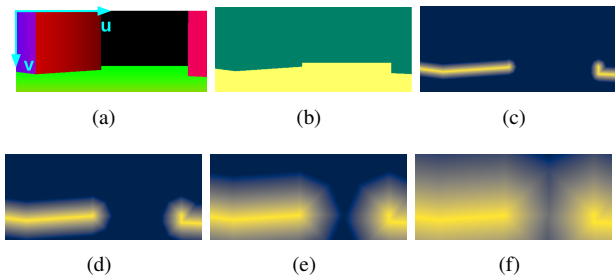


Fig. 6. Illustrations in Gazebo simulation. (a) Surface normal image; (b) Binary navigable space segmentation (the same color meaning as Fig. III-B.1) and different EDFs with varying scale factors of (c) $\alpha = 0.05$, (d) $\alpha = 0.25$, (e) $\alpha = 0.55$ and (f) $\alpha = 1.00$.

2) *Target Progress*: To evaluate target progress during the navigation progress, we propose to use the distance on $SE(3)$ as the metric. We define three types of frames: world frame F_w , primitive pose frame F_{pj} , and goal frame F_g . The transformation of F_{pj} in F_w is denoted as \mathbf{T}_{wpj} while that of F_g in F_w is \mathbf{T}_{wg} . A typical approach to represent the distance is to split a pose into a position and an orientation and define two distances on \mathbb{R}^3 and $SO(3)$. Then the two distances can be fused in a weighted manner with two strictly positive scaling factors a and b and with an exponent parameter $p \in [1, \infty]$ [58]:

$$d(\mathbf{T}_{wpj}, \mathbf{T}_{wg}) = [a \cdot d_{rot}(\mathbf{R}_{wpj}, \mathbf{R}_{wg})^p + b \cdot d_{trans}(\mathbf{t}_{wpj}, \mathbf{t}_{wg})^p]^{1/p}. \quad (12)$$

We use the Euclidean distance as $d_{trans}(\mathbf{t}_{wpj}, \mathbf{t}_{wg})$, the Riemannian distance over $SO(3)$ as $d_{rot}(\mathbf{R}_{wpj}, \mathbf{R}_{wg})$ and set p as 2. Then the distance (target cost) between two transformation matrices can be defined [59] as:

$$c_t^j = d(\mathbf{T}_{wpj}, \mathbf{T}_{wg}) = \left[a \cdot \left\| \log(\mathbf{R}_{wpj}^{-1} \mathbf{R}_{wg}) \right\|^2 + b \cdot \left\| \mathbf{t}_{wpj} - \mathbf{t}_{wg} \right\|^2 \right]^{1/2}. \quad (13)$$

IV. EXPERIMENTS

A. Segmentation Performance

Datasets: We evaluate the proposed method on the standard KITTI road benchmark [60]. The original data contains 289 training images (with ground-truth (gt) labels) and 290 testing images (without gt labels). Since our proposed method is designed to learn the segmentation from images in a self-supervised manner, we can only learn free space from the images without overly ambiguous boundaries such that the learned structure can be consistent with human-defined labels. Otherwise, the self-learned segmentation will be different from the gt labels (but still reasonable), causing confusion for evaluation. Therefore, throughout the experiments (including the baseline experiments), we only use the images starting with *um* and *umm* with corresponding *road* (instead of *lane*) gt labels in training data and split them into three subsets, (a) training (131 images); (b) validation (20 images) and (c) testing (40 images). We use the processed LiDAR data as the depth images and the SNE (surface normal estimation) module proposed in [6] to compute the surface normal images.

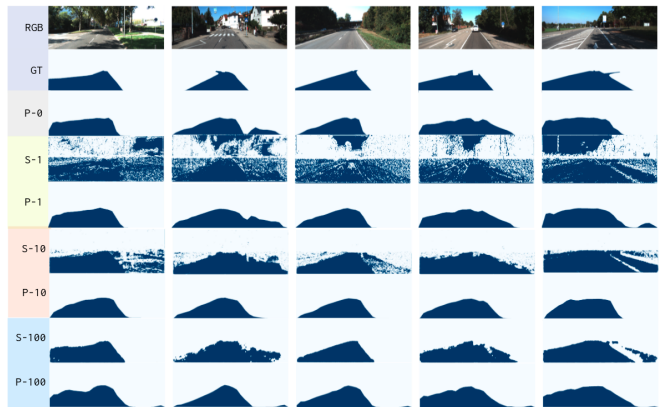


Fig. 7. Qualitative results on KITTI road benchmark. First row: RGB images; Second row: ground-truth navigable space segmentation. Label for each row of prediction results (from the third to the last row), S/P-#: S represents the baseline method, SNE-RoadSeg [6]; P represents the proposed method, PSV-Nets; # represents the percentage of the used gt labels. Note: the baseline method will not work if no gt labels are provided, thus S-0 is not available.

Implementation Details: To implement the PSV-Nets as illustrated in Fig. 1, E1 is a U-Net [61] with 2D convolution kernels and D1 is a simple fully convolutional network. Similar to [52], IFE in E2 is a VGG-16 network up to layer *conv5_4* and we use the concatenation of features from layer *conv2_3*, *conv3_3*, *conv4_3* and *conv5_4* as the visual features of the nodes in the graph. The GCN in E2 has been introduced in Fig. 3. We use the mesh renderer proposed in [53] as the D2 (NR). Only E1, D1 and E2 have parameters that need to be learned. We use the *Adam optimizer* for both nets and set the learning rate $lr_1 = 1e-3$ for Net-I and $lr_2 = 1e-4$ for Net-II. The batch size is 1. The total number of training epoch is 15, and we fix the weights of Net-I after epoch 3. We set the weights in \mathcal{L}_2 (Eq. (5)) as $\lambda_1 = 0.8$ and $\lambda_2 = 0.2$. We implement the whole framework using PyTorch [62] and conduct all experiments on a single Nvidia Geforce RTX 2080 Super GPU.

Evaluation Metrics: We compare to the most recent baseline [6], a fully supervised learning based state-of-the-art method for predicting navigable space. We use the same metrics, i.e., Accuracy, Precision, Recall, F-Score, and IoU (Intersection over Union). The definition of the metrics are: $\mathbf{A} = \frac{n_{tp} + n_{tn}}{n_{tp} + n_{tn} + n_{fp} + n_{fn}}$, $\mathbf{P} = \frac{n_{tp}}{n_{tp} + n_{fp}}$, $\mathbf{R} = \frac{n_{tp}}{n_{tp} + n_{fn}}$, $\mathbf{F} = \frac{2n_{tp}^2}{2n_{tp}^2 + n_{tp}(n_{fp} + n_{fn})}$, and $\mathbf{I} = \frac{n_{tp}}{n_{tp} + n_{fp} + n_{fn}}$, where n_{tp} , n_{tn} , n_{fp} and n_{fn} are true positive, true negative, false positive and false negative, respectively. We set the same parameters for the two methods for fair comparisons.

Analysis: A qualitative comparison between the proposed method with the baseline method is shown in Fig. 7, where predictions are shown with 4 different percentages of gt labels: 0%, 1%, 10%, and 100%. We can see *the proposed PSV-Nets can predict results close to the gt labels even without any gt labels provided during training (the third row)*. Both models can achieve better predictions as the number of gt labels becomes larger. However, we can still observe the advantage of our PSV-Nets over the baseline

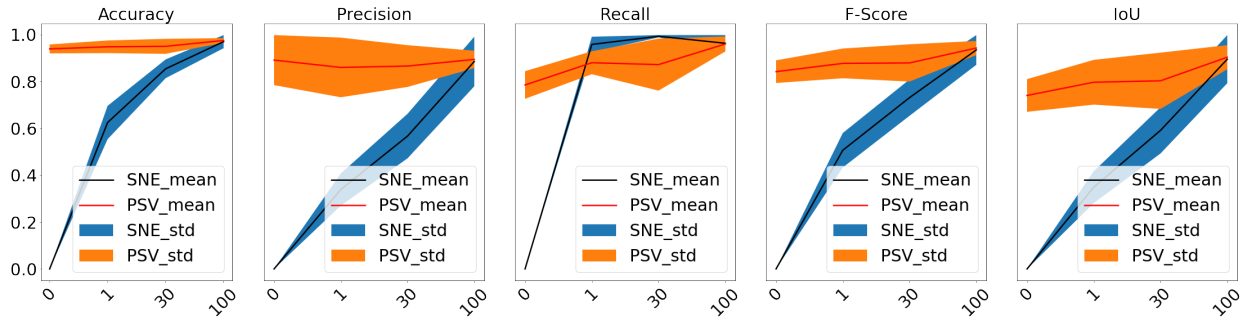


Fig. 8. Quantitative results on KITTI road benchmark. The horizontal axis represents the percentage of the used gt labels (only the data of 4 percentages are shown: 0, 1, 30, and 100). The statistical results are computed from all of the 40 images in testing data.

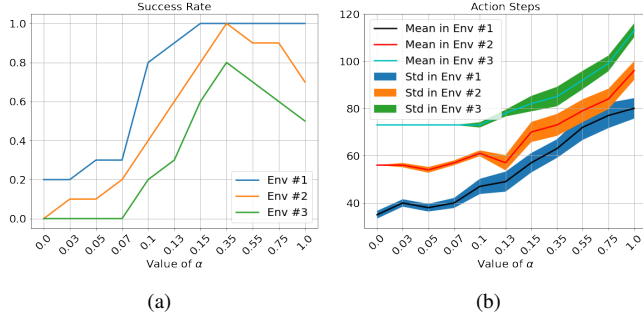


Fig. 9. Navigation behaviors comparison with different values of α in multiple maps.

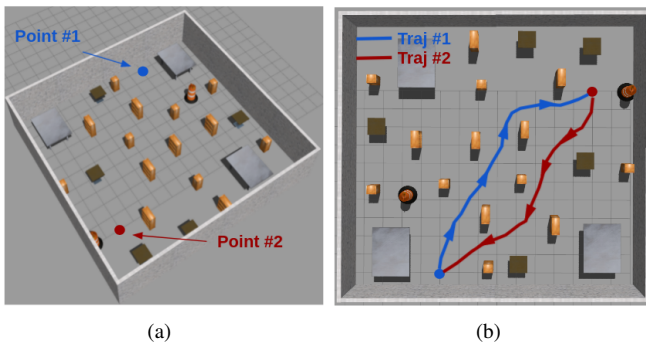


Fig. 10. Navigation in a cluttered room environment with random furniture. Demonstrations are provided in the supplementary video.

method at all listed levels of gt percentages (even when 100% of the gt labels are available). A more detailed comparison can be seen in Fig. 8.

B. Planning Performance

To show the effectiveness of the proposed SEDF navigation component, we first design three maps with varying sizes in the Gazebo simulator: *Env #1* ($3m \times 3m$), *Env #2* ($5m \times 5m$), and *Env #3* ($7m \times 7m$) (map design details can be seen in the supplementary video). We randomly place cubic obstacles in the environment and the number of obstacles is proportional to the size of the map. The larger the map is, the more cluttered the environment is. Different values of α (Eq. (10)) result in different SEDF images (Fig. 6) and further affect collision avoidance during navigation. We sample 11 values of α and run 10 trials of goal-oriented (from origin to the map diagonal corner) navigation on each

α value in each map, and compute the success rate (Fig. 9(a)) and the required action steps (Fig. 9(b)).

It can be seen in Fig. 9(a) that the success rate is generally proportional to the value of α , particularly when $\alpha \in [0.07, 0.35]$. If α is too small, say < 0.07 , it means the valid region of obstacle gradients is too limited (e.g., see Fig. 6(c)), thus the risk is higher for the robot to collide with obstacles, leading to a low success rate. In contrast, if the α value is too large (e.g., > 0.35), then the obstacle gradients will be propagated to the whole image and this results in a too narrow free space to navigate through (see Fig. 6(e) and Fig. 6(f)). In simulation the robot can be easily stuck during navigation especially when the environment is very cluttered. This can be seen from Fig. 9(a) that the success rate in a less-cluttered environment (e.g., *Env #1*) can still remain high with large α values while the rate is decreasing if the clutteredness of the environment (e.g., *Env #3*) is increasing.

In Fig. 9(b), we can see that the larger the environment is, the more action steps are required. It is also interesting to observe that the numbers of required action steps in all maps are also proportional to the value of α . This is because if α is small, the clearance distance to obstacles might be small while the robot passes by the obstacles to move toward the goal, thus the trajectory length might be short. On the other hand, if the value of α is large, the robot will always try to stay as far as possible from obstacles and this will cause long detours.

To further validate our proposed visual navigation system, we design a larger and more cluttered environment, as shown in Fig. 10(a), where two ending points are marked as Point #1 and Point #2. The robot will first navigate from Point #1 to Point #2 and then move in a reverse direction. The two trajectories are marked in Fig. 10(b) as Traj #1 and Traj #2, respectively. Demonstrations are provided as supplementary materials.

V. CONCLUSION

We propose a new framework, PSV-Nets, to learn the navigable space in an unsupervised fashion. The proposed framework discretizes the boundary of navigable spaces into a set of vertices. We then present a local navigation planning framework to guide the robot to navigate with the output of PSV-Nets. With extensive evaluations, we have validated the effectiveness of the proposed method and the remarkable

advantages over the state-of-the-art fully supervised learning baseline method.

REFERENCES

- [1] Zhi Tian, Tong He, Chunhua Shen, and Youliang Yan. Decoders matter for semantic segmentation: Data-dependent decoding enables flexible feature aggregation. In *Proceedings of the IEEE/CVF Conference on Computer Vision and Pattern Recognition*, pages 3126–3135, 2019.
- [2] Weiyue Wang and Ulrich Neumann. Depth-aware cnn for rgb-d segmentation. In *Proceedings of the European Conference on Computer Vision (ECCV)*, pages 135–150, 2018.
- [3] Maoke Yang, Kun Yu, Chi Zhang, Zhiwei Li, and Kuiyuan Yang. Denseaspp for semantic segmentation in street scenes. In *Proceedings of the IEEE conference on computer vision and pattern recognition*, pages 3684–3692, 2018.
- [4] Maggie Wigness, Sungmin Eum, John G Rogers, David Han, and Heesung Kwon. A rugd dataset for autonomous navigation and visual perception in unstructured outdoor environments. In *2019 IEEE/RSJ International Conference on Intelligent Robots and Systems (IROS)*, pages 5000–5007. IEEE, 2019.
- [5] Satoshi Tsutsui, Tommi Kerola, Shunta Saito, and David J Crandall. Minimizing supervision for free-space segmentation. In *Proceedings of the IEEE Conference on Computer Vision and Pattern Recognition Workshops*, pages 988–997, 2018.
- [6] Rui Fan, Hengli Wang, Peide Cai, and Ming Liu. Sne-roadseg: Incorporating surface normal information into semantic segmentation for accurate freespace detection. In *European Conference on Computer Vision*, pages 340–356. Springer, 2020.
- [7] Satoshi Tsutsui, Tommi Kerola, and Shunta Saito. Distantly supervised road segmentation. In *Proceedings of the IEEE International Conference on Computer Vision Workshops*, pages 174–181, 2017.
- [8] Fabio Pizzati and Fernando García. Enhanced free space detection in multiple lanes based on single cnn with scene identification. In *2019 IEEE Intelligent Vehicles Symposium (IV)*, pages 2536–2541. IEEE, 2019.
- [9] Hengli Wang, Rui Fan, Yuxiang Sun, and Ming Liu. Applying surface normal information in drivable area and road anomaly detection for ground mobile robots. *arXiv preprint arXiv:2008.11383*, 2020.
- [10] Divya Kothandaraman, Rohan Chandra, and Dinesh Manocha. Safe: Self-attention based unsupervised road safety classification in hazardous environments. *arXiv preprint arXiv:2012.08939*, 2020.
- [11] Andreas Geiger, Philip Lenz, Christoph Stiller, and Raquel Urtasun. Vision meets robotics: The kitti dataset. *The International Journal of Robotics Research*, 32(11):1231–1237, 2013.
- [12] Marius Cordts, Mohamed Omran, Sebastian Ramos, Timo Scharwächter, Markus Enzweiler, Rodrigo Benenson, Uwe Franke, Stefan Roth, and Bernt Schiele. The cityscapes dataset. In *CVPR Workshop on the Future of Datasets in Vision*, volume 2, 2015.
- [13] Christopher P Burgess, Loic Matthey, Nicholas Watters, Rishabh Kabra, Irina Higgins, Matt Botvinick, and Alexander Lerchner. Monet: Unsupervised scene decomposition and representation. *arXiv preprint arXiv:1901.11390*, 2019.
- [14] Klaus Greff, Raphaël Lopez Kaufman, Rishabh Kabra, Nick Watters, Christopher Burgess, Daniel Zoran, Loic Matthey, Matthew Botvinick, and Alexander Lerchner. Multi-object representation learning with iterative variational inference. In *International Conference on Machine Learning*, pages 2424–2433. PMLR, 2019.
- [15] Martin Engelcke, Adam R Kosiorek, Oivi Parker Jones, and Ingmar Posner. Genesis: Generative scene inference and sampling with object-centric latent representations. *arXiv preprint arXiv:1907.13052*, 2019.
- [16] Zhixuan Lin, Yi-Fu Wu, Skand Vishwanath Peri, Weihao Sun, Gautam Singh, Fei Deng, Jindong Jiang, and Sungjin Ahn. Space: Unsupervised object-oriented scene representation via spatial attention and decomposition. *arXiv preprint arXiv:2001.02407*, 2020.
- [17] Zian Wang, David Acuna, Huan Ling, Amlan Kar, and Sanja Fidler. Object instance annotation with deep extreme level set evolution. In *Proceedings of the IEEE/CVF Conference on Computer Vision and Pattern Recognition*, pages 7500–7508, 2019.
- [18] Sida Peng, Wen Jiang, Huaijin Pi, Xiuli Li, Hujun Bao, and Xiaowei Zhou. Deep snake for real-time instance segmentation. In *Proceedings of the IEEE/CVF Conference on Computer Vision and Pattern Recognition*, pages 8533–8542, 2020.
- [19] Lluis Castrejon, Kaustav Kundu, Raquel Urtasun, and Sanja Fidler. Annotating object instances with a polygon-rnn. In *Proceedings of the IEEE conference on computer vision and pattern recognition*, pages 5230–5238, 2017.
- [20] David Acuna, Huan Ling, Amlan Kar, and Sanja Fidler. Efficient interactive annotation of segmentation datasets with polygon-rnn++. In *Proceedings of the IEEE conference on Computer Vision and Pattern Recognition*, pages 859–868, 2018.
- [21] Huan Ling, Jun Gao, Amlan Kar, Wenzheng Chen, and Sanja Fidler. Fast interactive object annotation with curve-gcn. In *Proceedings of the IEEE/CVF Conference on Computer Vision and Pattern Recognition*, pages 5257–5266, 2019.
- [22] Kamyar Nazeri, Eric Ng, Tony Joseph, Faisal Z Qureshi, and Mehran Ebrahimi. Edgeconnect: Generative image inpainting with adversarial edge learning. *arXiv preprint arXiv:1901.00212*, 2019.
- [23] Eric Jang, Shixiang Gu, and Ben Poole. Categorical reparameterization with gumbel-softmax. *arXiv preprint arXiv:1611.01144*, 2016.
- [24] Michael Kass, Andrew Witkin, and Demetri Terzopoulos. Snakes: Active contour models. *International journal of computer vision*, 1(4):321–331, 1988.
- [25] Diego Marcos, Devis Tuia, Benjamin Kellenberger, Lisa Zhang, Min Bai, Renjie Liao, and Raquel Urtasun. Learning deep structured active contours end-to-end. In *Proceedings of the IEEE Conference on Computer Vision and Pattern Recognition*, pages 8877–8885, 2018.
- [26] Fuyang Zhang, Nelson Nauata, and Yasutaka Furukawa. Convmpn: Convolutional message passing neural network for structured outdoor architecture reconstruction. In *Proceedings of the IEEE/CVF Conference on Computer Vision and Pattern Recognition*, pages 2798–2807, 2020.
- [27] Xu Chen, Bryan M Williams, Srinivasa R Vallabhaneni, Gabriela Czanner, Rachel Williams, and Yalin Zheng. Learning active contour models for medical image segmentation. In *Proceedings of the IEEE/CVF Conference on Computer Vision and Pattern Recognition*, pages 11632–11640, 2019.
- [28] Dominic Cheng, Renjie Liao, Sanja Fidler, and Raquel Urtasun. Darnet: Deep active ray network for building segmentation. In *Proceedings of the IEEE/CVF Conference on Computer Vision and Pattern Recognition*, pages 7431–7439, 2019.
- [29] Mickaël Chen, Thierry Artières, and Ludovic Denoyer. Unsupervised object segmentation by redrawing. *arXiv preprint arXiv:1905.13539*, 2019.
- [30] Michael Tschannen, Olivier Bachem, and Mario Lucic. Recent advances in autoencoder-based representation learning. *arXiv preprint arXiv:1812.05069*, 2018.
- [31] Yoshua Bengio, Aaron Courville, and Pascal Vincent. Representation learning: A review and new perspectives. *IEEE transactions on pattern analysis and machine intelligence*, 35(8):1798–1828, 2013.
- [32] Diederik P Kingma and Max Welling. Auto-encoding variational bayes. *arXiv preprint arXiv:1312.6114*, 2013.
- [33] Kihyuk Sohn, Honglak Lee, and Xinchen Yan. Learning structured output representation using deep conditional generative models. *Advances in neural information processing systems*, 28:3483–3491, 2015.
- [34] Ilya Tolstikhin, Olivier Bousquet, Sylvain Gelly, and Bernhard Schölkopf. Wasserstein auto-encoders. *arXiv preprint arXiv:1711.01558*, 2017.
- [35] Irina Higgins, Loic Matthey, Arka Pal, Christopher Burgess, Xavier Glorot, Matthew Botvinick, Shakir Mohamed, and Alexander Lerchner. beta-vae: Learning basic visual concepts with a constrained variational framework. 2016.
- [36] Yuri Burda, Roger Grosse, and Ruslan Salakhutdinov. Importance weighted autoencoders. *arXiv preprint arXiv:1509.00519*, 2015.
- [37] Emilien Dupont. Learning disentangled joint continuous and discrete representations. *arXiv preprint arXiv:1804.00104*, 2018.
- [38] Aaron van den Oord, Oriol Vinyals, and koray kavukcuoglu. Neural discrete representation learning. In I. Guyon, U. V. Luxburg, S. Bengio, H. Wallach, R. Fergus, S. Vishwanathan, and R. Garnett, editors, *Advances in Neural Information Processing Systems*, volume 30. Curran Associates, Inc., 2017.
- [39] Justin Liang, Namdar Homayounfar, Wei-Chiu Ma, Yuwen Xiong, Rui Hu, and Raquel Urtasun. Polytransform: Deep polygon transformer for instance segmentation. In *Proceedings of the IEEE/CVF Conference on Computer Vision and Pattern Recognition (CVPR)*, June 2020.
- [40] David Acuna, Amlan Kar, and Sanja Fidler. Devil is in the edges: Learning semantic boundaries from noisy annotations. 2019.

- [41] Mingmin Zhen, Jinglu Wang, Lei Zhou, Shiwei Li, Tianwei Shen, Jiayang Shang, Tian Fang, and Long Quan. Joint semantic segmentation and boundary detection using iterative pyramid contexts. In *Proceedings of the IEEE/CVF Conference on Computer Vision and Pattern Recognition (CVPR)*, June 2020.
- [42] Dmitrii Marin, Zijian He, Peter Vajda, Priyam Chatterjee, Sam Tsai, Fei Yang, and Yuri Boykov. Efficient segmentation: Learning down-sampling near semantic boundaries. In *Proceedings of the IEEE/CVF International Conference on Computer Vision (ICCV)*, October 2019.
- [43] William B Shen, Danfei Xu, Yuke Zhu, Leonidas J Guibas, Li Fei-Fei, and Silvio Savarese. Situational fusion of visual representation for visual navigation. In *Proceedings of the IEEE/CVF International Conference on Computer Vision*, pages 2881–2890, 2019.
- [44] Somil Bansal, Varun Tolani, Saurabh Gupta, Jitendra Malik, and Claire Tomlin. Combining optimal control and learning for visual navigation in novel environments. In *Conference on Robot Learning*, pages 420–429. PMLR, 2020.
- [45] Travis Manderson, Juan Camilo Gamboa Higuera, Stefan Wapnick, Jean-François Tremblay, Florian Shkurti, David Meger, and Gregory Dudek. Vision-based goal-conditioned policies for underwater navigation in the presence of obstacles. *arXiv preprint arXiv:2006.16235*, 2020.
- [46] Noriaki Hirose, Shun Taguchi, Fei Xia, Roberto Martin-Martin, Yasumasa Tahara, Masanori Ishigaki, and Silvio Savarese. Probabilistic visual navigation with bidirectional image prediction. *arXiv preprint arXiv:2003.09224*, 2020.
- [47] Saurabh Gupta, James Davidson, Sergey Levine, Rahul Sukthankar, and Jitendra Malik. Cognitive mapping and planning for visual navigation. In *Proceedings of the IEEE Conference on Computer Vision and Pattern Recognition*, pages 2616–2625, 2017.
- [48] Devendra Singh Chaplot, Ruslan Salakhutdinov, Abhinav Gupta, and Saurabh Gupta. Neural topological slam for visual navigation. In *Proceedings of the IEEE/CVF Conference on Computer Vision and Pattern Recognition*, pages 12875–12884, 2020.
- [49] Saurabh Gupta, David Fouhey, Sergey Levine, and Jitendra Malik. Unifying map and landmark based representations for visual navigation. *arXiv preprint arXiv:1712.08125*, 2017.
- [50] Yi Wu, Yuxin Wu, Aviv Tamar, Stuart Russell, Georgia Gkioxari, and Yuandong Tian. Bayesian relational memory for semantic visual navigation. In *Proceedings of the IEEE/CVF International Conference on Computer Vision*, pages 2769–2779, 2019.
- [60] Jannik Fritsch, Tobias Kuehnl, and Andreas Geiger. A new performance measure and evaluation benchmark for road detection al-
- [51] Vitor Guizilini, Rares Ambrus, Sudeep Pillai, Allan Raventos, and Adrien Gaidon. 3d packing for self-supervised monocular depth estimation. In *Proceedings of the IEEE/CVF Conference on Computer Vision and Pattern Recognition*, pages 2485–2494, 2020.
- [52] Nanyang Wang, Yinda Zhang, Zhuwen Li, Yanwei Fu, Wei Liu, and Yu-Gang Jiang. Pixel2mesh: Generating 3d mesh models from single rgb images. In *Proceedings of the European Conference on Computer Vision (ECCV)*, pages 52–67, 2018.
- [53] Hiroharu Kato, Yoshitaka Ushiku, and Tatsuya Harada. Neural 3d mesh renderer. In *Proceedings of the IEEE conference on computer vision and pattern recognition*, pages 3907–3916, 2018.
- [54] Thomas M Howard and Alonzo Kelly. Optimal rough terrain trajectory generation for wheeled mobile robots. *The International Journal of Robotics Research*, 26(2):141–166, 2007.
- [55] Thomas M Howard, Colin J Green, Alonzo Kelly, and Dave Ferguson. State space sampling of feasible motions for high-performance mobile robot navigation in complex environments. *Journal of Field Robotics*, 25(6-7):325–345, 2008.
- [56] Fei Gao, Yi Lin, and Shaojie Shen. Gradient-based online safe trajectory generation for quadrotor flight in complex environments. In *2017 IEEE/RSJ international conference on intelligent robots and systems (IROS)*, pages 3681–3688. IEEE, 2017.
- [57] Luxin Han, Fei Gao, Boyu Zhou, and Shaojie Shen. Fiesta: Fast incremental euclidean distance fields for online motion planning of aerial robots. In *2019 IEEE/RSJ International Conference on Intelligent Robots and Systems (IROS)*, pages 4423–4430. IEEE, 2019.
- [58] Romain Brégier, Frédéric Devernay, Laetitia Leyrit, and James L Crowley. Defining the pose of any 3d rigid object and an associated distance. *International Journal of Computer Vision*, 126(6):571–596, 2018.
- [59] Frank C Park. Distance metrics on the rigid-body motions with applications to mechanism design. 1995. algorithms. In *16th International IEEE Conference on Intelligent Transportation Systems (ITSC 2013)*, pages 1693–1700. IEEE, 2013.
- [61] Olaf Ronneberger, Philipp Fischer, and Thomas Brox. U-net: Convolutional networks for biomedical image segmentation. In *International Conference on Medical image computing and computer-assisted intervention*, pages 234–241. Springer, 2015.
- [62] Adam Paszke, Sam Gross, Soumith Chintala, Gregory Chanan, Edward Yang, Zachary DeVito, Zeming Lin, Alban Desmaison, Luca Antiga, and Adam Lerer. Automatic differentiation in pytorch. 2017.